Original Article

The effect of porosity on strain evolution and failure of soldered, small-diameter, thin-walled metallic pipes

Sophie A.M. McNair [a,], Jiraphant Srisuriyachot [a], Samuel Omole [a], Thomas Connolley [b], Andrew Rhead [a], Alexander J.G. Lunt [a]*

[a] *University of Bath, GB, UK*
[b] *Diamond Light Source, GB, UK*

ABSTRACT

Small-diameter, thin-walled pipes have applications in a wide range of industries including high-energy physics, heat transfer, nuclear, medical and communications. There are no standards that exist for welds less than 0.5 mm in width, and as such it is difficult to determine the likely performance of a thin-walled pipe weld. Porosity is largely inevitable in fusion welded joints and is a determining factor in the performance of a connection.

This study focused on characterisation of the evolution of strains in soldered welds less than 0.5 mm in width, by incrementally tensile loading samples and studying them in-situ with Synchrotron X-Ray Computed Tomography and X-Ray Diffraction. Two sample geometries were studied, and porosity defects were present in both, although the levels of porosity size, number and area varied dramatically between the two samples.

Lattice strain interpretation showed that crack propagation for such samples is not driven by porosity but that crack evolution occurs at the same location and load levels irrespective of the presence of pores. Residual stresses of up to 0.3% from the fusion welding process were seen in both samples and appear to have a greater impact on locations of failure than porosity. Porosity does cause differences in strains across directions, however high strains alone did not appear to cause premature failure. Hence, efforts to improve weld strength should in future focus more on reducing residual stresses than reducing porosity.

1. Introduction

The use of small-diameter, thin-walled, metallic tubes, or pipes, have increased dramatically over recent years due to advances in manufacturing techniques. They have become a key value-adding factor in a number of industries such as: particle physics, nuclear energy generation, medical science and mobile communications by allowing the production of smaller components and supporting tighter tolerances [1—4].

However, many applications of such thin-walled pipes require the use of piping longer than can be manufactured, or compatibility with other components of differing diameters or materials [5,6]. Therefore, joining thin-walled pipes is commonly required, and strong, reliable joints are crucial for the uptake of thin-walled pipes within industry.

Due to the relatively new application of thin-walled pipes within industry, there are few qualitative studies on joining methods and how to control parameters to ensure an effective joint on a smaller scale [7]. However, soldering is a common joining method that has promising compatibility with thin-walled pipes as it is frequently used to create very thin bonds between components, such as for electronics applications [8—11]. Soldering is also an appropriate choice when joining dissimilar materials [12,13], complex geometries [14], and it is a method which is well established for larger diameter piping [15,16].

During the soldering process a filler material is heated and melted using an appropriate heat source, and the solidification of the solder creates a strong bond between the two surfaces to be joined. This method is very similar to brazing, however in contrast to this method the melting point of solders are limited to less than 450 °C [17]. Several factors can affect the quality of a soft soldered joint including porosity or cracks in the solder, incomplete bonding at the solder/substrate interface or too much/too little filler material. As such, the joining parameters must be carefully designed and continuously controlled to ensure a strong and reliable joint [18].

The standards that exist to assess the quality of a soldered joint require a minimum joint thickness of 0.5 mm, which is typically several times larger than the average thin-walled pipe joint [19—21]. Previous studies have indicated that the in-service performance of fusion welded components depends on microstructural features across length scales [22] however this has not yet been properly defined within engineering standards. As such, it is difficult to determine the limits on permitted defects or flaws for thin-walled pipe joints and designers tend to be over-cautious. This can lead to higher production costs, delays in manufacture in addition to a lack of confidence in thin-walled pipe connections.

Solder voids, or porosity, are an almost inevitable defect or flaw that can occur within solder joints, that are generally caused by the heating process of the filler material [23]. The addition of heat can cause evaporation and entrapment of gases in the solder, or alternatively gases can arise from metallisation reactions between the filler material, substrate and/or substrate coating [24]. Voids have been shown to have a negative impact on the reliability of soldered joints, although this is dependent on both the size, frequency and location of this type of defect [25]. Larger voids directly affect the mechanical strength of the joint due to a reduction in solder area [26], whereas if several smaller voids exist close to one another, there is a higher probability of crack propagation and subsequent failure [27].

This work aims to determine the effects porosity has on the strength, load response and failure mode of soft-soldered, thin-walled pipe joints using high-energy synchrotron radiation. Synchrotron X-Ray Diffraction (SXRD) is a powerful technique used to characterise position of atoms within materials and the spacing between atomic planes [28]. By incrementally loading samples and studying the SXRD patterns in-situ, the evolution of lattice strain can be obtained and localised regions of high strain can be identified [29]. Synchrotron radiation is also an excellent source of radiation for tomographic imaging as it is high intensity and spatially coherent [30] which can create highly spatially resolved images (microscale pixel sizes) [31]. Synchrotron X-Ray Computed Tomography (SXCT) involves recording a series of 2D radiographs which are then reconstructed into a 3D image [32]. This 3D image is recorded in-situ and directly compared to the areas of high lattice strain as per SXRD experiments, with no need to remove loading from the sample. Due to its high resolution, synchrotron characterisation is of increasing interest in the study of cracking and other failures induced by porosity, precipitates and intermetallic inclusions, as well as grain structure of metallic materials, as previously demonstrated by Wu et al. [33].

The main application drive for this work is the use of thin-walled pipes for use inside accelerator physics particle detectors. In particular, thin-walled, stainless steel pipes will be used in two-phase CO_2 cooling for the Compact Muon Solenoid (CMS) tracker upgrade at CERN, Switzerland [34]. Thin-walled pipes have been chosen as they allow effective heat transfer, reduce the mass of the system (and the associated shadowing in particle detection) [35], and allow the high pressures required for effective two-phase CO_2 cooling [36]. However, the cooling system will be several kilometres in length and the limiting geometry of this design mean that soldered joints are required to be an integral part of the cooling structure. In addition to these mechanical strength demands, the detector will be in place for over 10 years with no planned maintenance, and as such reliability of joints is key for long-term success.

2. Methodology

2.1. Sample preparation

Two different samples were prepared for this experiment, representing designs that will be used in two different modules, the PS and 2 S [37]. The first sample (designated TBPS) is a 38 mm long capillary tube, with outer diameter 2 mm and wall thickness 0.5 mm. The parent material for the sample tube is stainless steel 316 L, with a CuNi coating. The thin-walled pipe was then attached at both ends to a CuNi stud and grip, using a soft soldered Sn62Pb36Ag2 flux. To ensure one joint would predictably and reliably fail before the other, one end of the pipe was soldered with a 3 mm overlap, while the other was 10 mm. A schematic cross section of the test sample is shown in Fig. 1a.

The second sample (designated TB2S) was made up of a CuNi 70/30 stud soft soldered to a grip of the same material, with a 3 mm overlap, also using Sn62Pb36Ag2 flux. The grip had an outer diameter of 3 mm and a wall thickness of 0.75 mm. This geometry is shown in more detail in Fig. 1b.

For both samples a 15 mm M6 male threaded grip is attached at each end to hold the sample securely in place in the load cell and provide the tensile loading.
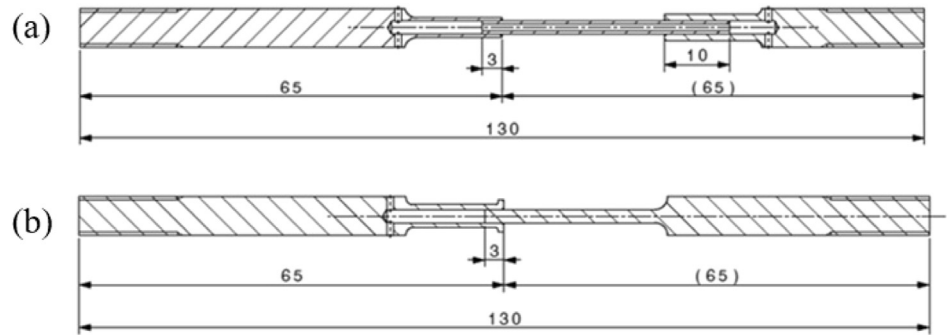
Fig. 1 — TBPS sample configuration (a) and TB2S sample configuration (b).

2.2. Experimental set-up

In-situ tests were performed on the I12 beamline at Diamond Light Source, UK. A Deben CT5000 5 kN load cell (Deben, UK) was used to perform tensile loading of the sample, in a displacement control mode. The load cell was held stationary at each increment to facilitate radiograph and transmission X-Ray Powder Diffraction (XRD) pattern collection.

Monochromatic tomography was performed using a beam energy of 120 keV (wavelength = 0.10 Å). Samples were rotated between −90° and 90° in increments of 0.1° with an exposure time of 0.25 s per point. A high-resolution PCO. edge imaging camera (PCO, Germany) recorded radiographs with a pixel size of $1.3 \times 1.3 \ \mu m^2$ and a field of view of $3.3 \times 2.8 \ mm^2$ (2540×2150 pixels). To facilitate through-average 2D strain mapping, a $50 \times 50 \ \mu m^2$ collimated 120 keV beam was used. A Pilatus 2 M CdTe 2 M detector (Dectris, Switzerland) was mounted offset to the imaging camera in the x-direction and was translated into the central position to record 2D diffraction patterns at each load increment.

For the SXRD collection, the sample was rastered across the beam to form a grid array, with measurements taken at points 200 μm apart in both the x and y directions to capture localised strain effects. Between each scan, a tensile load was applied at a strain rate of 0.1 mm/min. Data collection was taken at set displacements to allow comparison of performance between the two sample types. A custom grip system was designed and manufactured in house for the Deben CT5000, this allowed the load cell to provide tensile load and hold this load at a set displacement for the duration of the data collection. Fig. 2 shows the detector arrangement as well as a TBPS sample from the experiment before loading, with the top section of the Deben load cell removed for clarity, as well as the detector arrangement. Fig. 3 shows an overall schematic of the test set up.

The SXRD data was calibrated using a Lanthanum Hexaboride (LaB$_6$) sample, and the sample to detector distance was determined to be 1146 mm. An exposure time of 20s was used to collect the SXRD data.
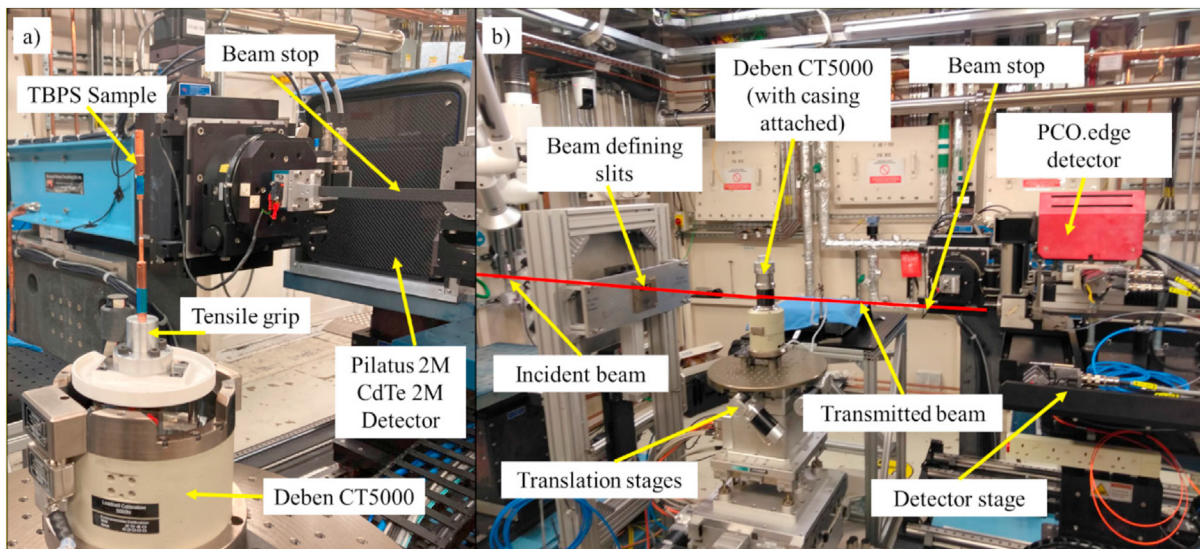

Fig. 2 — Images of test setup: a) upstream view of a TBPS sample secured into the bottom grip of the Deben load cell and diffraction detector. b) Side-view of setup showing incident and transmitted beam, translation stages, beam defining slits and tomography detector.
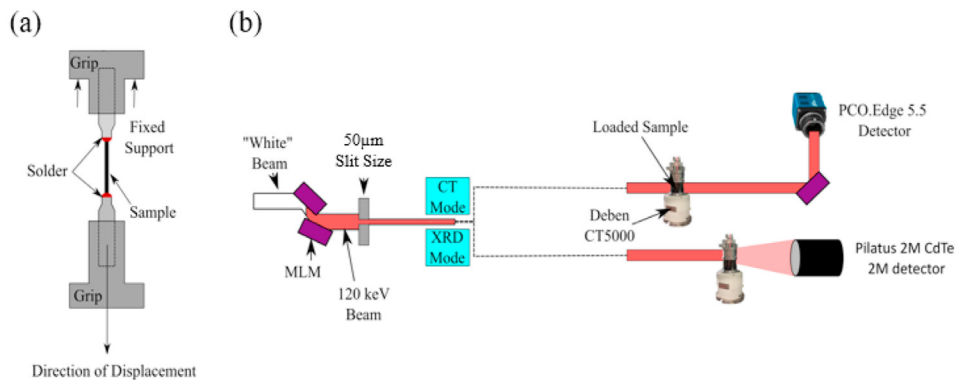
Fig. 3 − Geometry of grips used to provide tensile loading (a) and experimental set-up of beamline (b).

2.3. Synchrotron X-Ray Diffraction analysis

The SXRD data analysis was performed by reducing the 2D diffraction patterns into a 1D plot of intensity against scattering angle, which were subsequently fitted to provide estimates of the relevant peak centres. This process was performed using Data Analysis WorkbeNch (DAWN) software developed by Diamond Light Source [38,39]. Following the fitting of the peak centre from the calibration process, the diffraction patterns were reduced into plots of intensity against 2θ by azimuthal integration [40−42]. This was done both in the horizontal and vertical directions by defining the integration angles as shown in Fig. 4.

As can be seen from Fig. 4, for both orientations two arcs of 20° are taken across the respective axes known as the azimuthal range. The two arcs are then summed to give the intensity in this direction which can be used to resolve the strain in the vertical and horizontal directions, as these may be different upon loading.

The geometry of the sample meant that some points in the grid were 'off sample' and therefore an automated process using thresholding of the diffraction intensity was performed to identify these points within DAWN. This array of 'on' or 'off'

sample points were translated into real space, by comparing the x and y motor positions, to allow direct comparison between the XRD scans and tomographic images as summarised in Fig. 5.

To facilitate accurate peak fitting, the 1D azimuthal integration patterns were processed in DAWN using the following 'pipeline': Gaussian background subtraction, 1D crop of data at set 2θ values to highlight the peaks of interest and finally Pseudo-Voight fitting [43] to find the peak centres. Fig. 6 shows a 1D curve after a Gaussian background subtraction and 1D trimming, with the corresponding Miller indices of CuNi highlighted for each intensity peak [44].

DAWN allowed for batch processing of peak centre identification using the Pseudo-Voight fitting regime. After this, the peak centres in 2θ was converted to the crystal interplanar spacing (d) using the Bragg equation (Eq (1)).

$$2d\sin\theta = \lambda \tag{1}$$

where λ is the wavelength of the incident x-rays (0.10 Å) determined during calibration. CuNi is a Face Centred Cubic (FCC) crystal structure, and the following expression can be used to convert d to the lattice constant a.
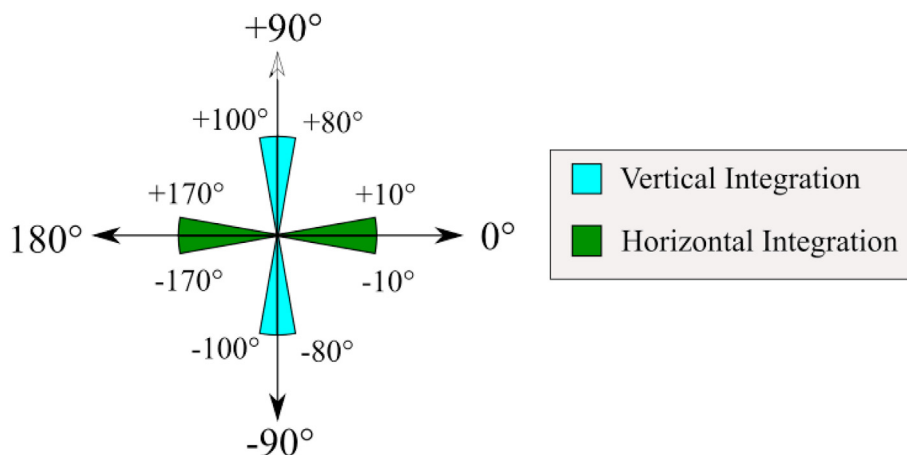

Fig. 4 − Azimuthal angle notation and angles used for vertical and horizontal integration.
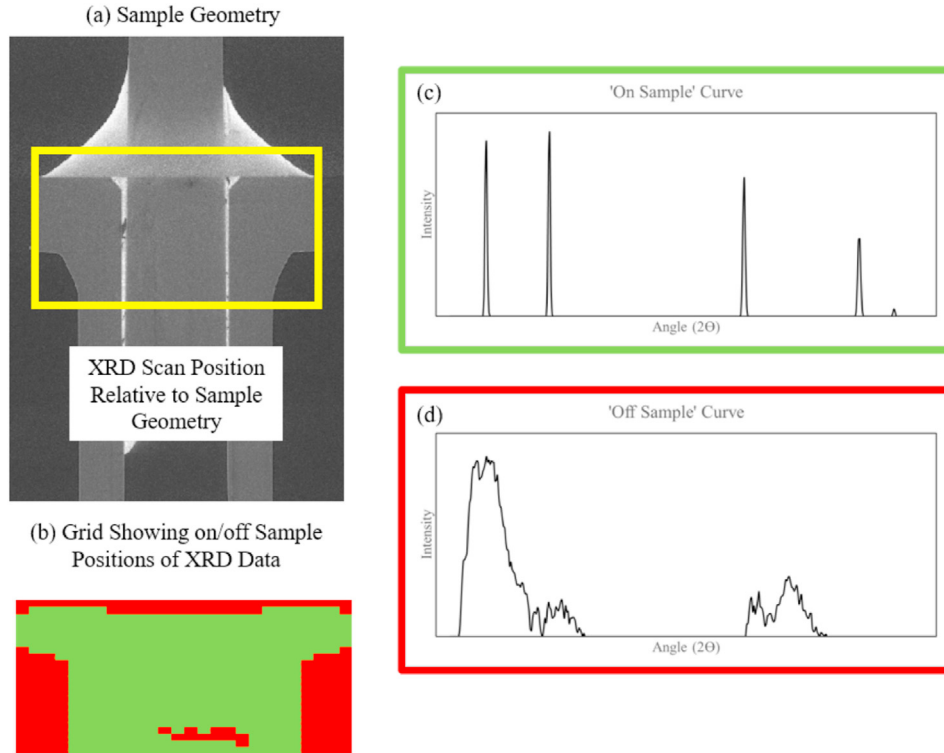
(a) Sample Geometry

XRD Scan Position Relative to Sample Geometry

(b) Grid Showing on/off Sample Positions of XRD Data

(c) 'On Sample' Curve

(d) 'Off Sample' Curve

Fig. 5 − (a) Sample geometry with SXRD positions bounding box highlighted (b) grid with SXRD data points either characterised as 'on sample' (green) or 'off sample' (red) (c) example 'on sample' curve and (d) example 'off sample' curve.

$$d_{hkl} = \frac{a}{\sqrt{h^2 + k^2 + l^2}} \tag{2}$$

where the constants h, k and l are taken from the crystal plane. For the plane (200), this equation simplifies to:

$$d_{200} = \frac{a}{\sqrt{2^2 + 0 + 0}} = \frac{a}{2} \tag{3}$$

CuNi has a nominal unstrained lattice parameter $(a_0) = 0.3534$ nm [45], which then allows for the given strain at any point to be calculated via.

$$strain = \frac{a - a_0}{a_0} \tag{4}$$

The given percentage strain from each data point was then converted into real space using the x and y motor positions at each data point to produce strain maps of the sample. Within the regions where solder was present the additional diffraction patterns associated with this phase were visible in the SXRD patterns. Fig. 7 shows an integrated SXRD pattern for the pure solder, with no CuNi peaks present.
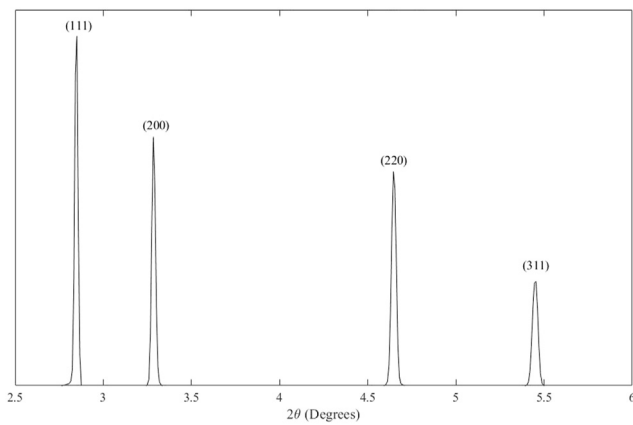

Fig. 6 − 1D SXRD curve taken from TB2S sample, with each peak corresponding to a crystal plane of CuNi 70/30 (highlighted).
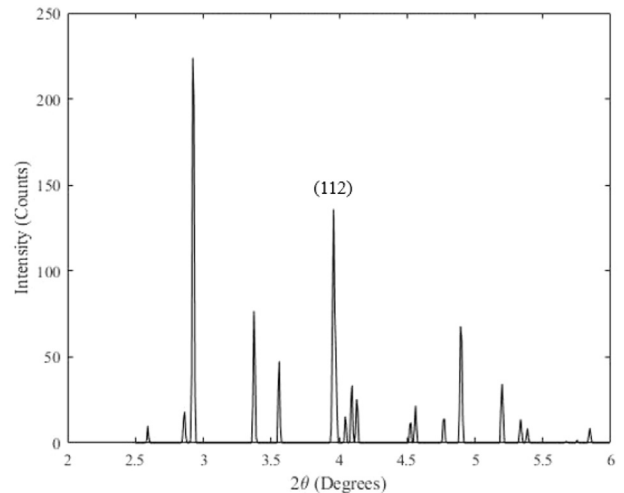

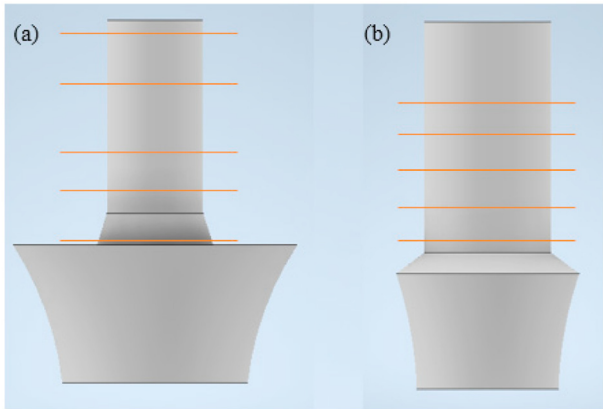**Fig. 7 − SXRD pattern of solder without CuNi peaks.**

Fig. 8 − Slice locations for 2D porosity evaluation for (a) TB2S and (b) TBPS samples.

To calculate the strain in the solder, the (112) peak was identified [46] as this peak was distinct from the CuNi curve and minimised any interaction between the two phases. In order to provide estimates of strain an average interplanar spacing d was found for the unloaded sample, and this d_0 was used to calculate the strain as per Eq (5).

$$strain\ in\ solder = \frac{(d - d_0)}{d_0} \quad (5)$$

2.4. Synchrotron X-Ray Computed Tomography analysis

3D reconstruction of the 2D SXCT data was carried out using Savu software (Diamond Light Source, UK) [47]. The images acquired during SXCT data collection are based on absorption of the incident X-rays, as described by Lambert-Beer's Law, Eq (6) [31].

$$I = I_0 e^{-\frac{\mu}{\rho}l} \quad (6)$$

where I_0 is the intensity of the incident X-rays, μ is the linear attenuation coefficient, ρ is the density of the material and l is the mass thickness of the material and I is the resulting intensity that reaches the detector.

When a sample is composed of different phases, the attenuation coefficients will vary with position which results in phase contrast in the image. However, the quality of the radiograph can also be affected by signal noise, beam hardening and scatter. Brightfield and darkfield correction of the resulting images was performed [48]. To remove artifacts in the data caused by beam hardening (where the average beam energy increases due to high density materials absorbing lower energy photons at a higher rate [49]) the beam was 'pre hardened' by passing the beam through 0.5 mm aluminium filters. These filters improve the image by removing low energy photons from the spectrum to create a more uniform higher energy spectrum incident beam [50].

2.5. Porosity analysis

To characterise the levels of porosity within the solder regions, the SXCT data was analysed using Avizo 9.2 (Thermo Fisher Scientific, USA). Regions of interest were identified at various points along the Z axis of the sample, Fig. 8.

These images were then transferred to ImageJ (LOCI, University of Wisconsin, USA) and assessed using the "analyze particles" function as shown in Fig. 9. This process generated information on number of pores, the area of each pore and the most significant dimension of each pore. The area of pores was summed to give the total area of porosity, and this was used to generate percentage porosity.

3. Results

3.1. SXCT failure mode analysis

Upon analysing the SXCT images, it was found that the TB2S sample has a significantly higher level of porosity than the TBPS sample], with some pores approaching the width of the solder material. Figs. 10 and 11 show the XCT images of the TB2S sample at progressive load increments, in the XY and XZ planes respectively. Comparing the unloaded state to 0.5 mm and 0.75 mm displacement it can be seen that failure starts to after an extension of 0.5 mm, with cracks appearing in the
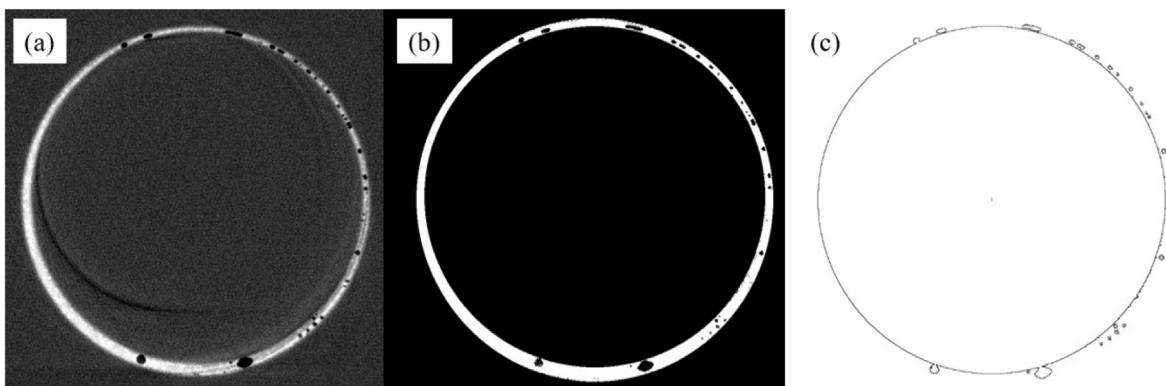

Fig. 9 − Porosity analysis process with (a) original image, (b) thresholded image and (c) particle analysis.
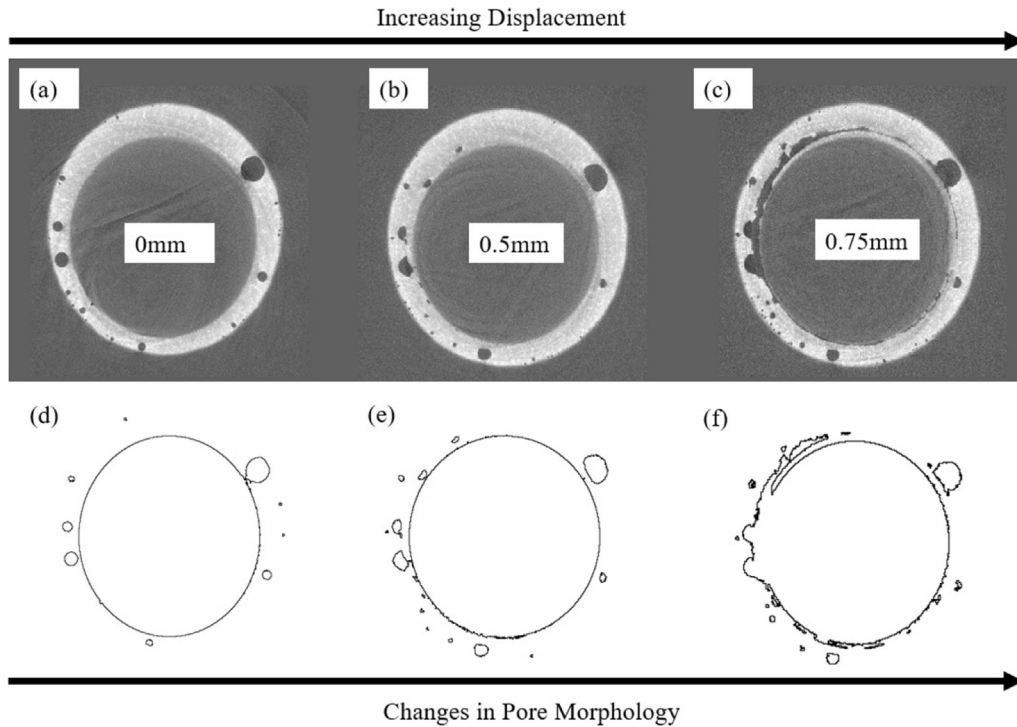
Fig. 10 − SXCT images of TB2S sample under progressive loading (a−c) with porosity outlined to demonstrate changed in morphology at different load increments (d−f).

horizonal direction and voids beginning to change in shape and widen.

Figs. 12 and 13 show the XCT images of the TBPS sample at progressive load increments, in the XY and XZ planes respectively. In these Figures, it can be seen that the solder distribution is more even, with significantly fewer pores. Despite this, failure occurs at the same elongation increment of 0.5 mm. In addition, the cracks propagate from the same location, close to the edge of the inner pipe, at both ends. This suggests that the crack propagation for the TB2S these samples are not solely driven by the porosity levels and that geometry has an important role to play in thin solder failure.

Since bonding strength of a soldered joint is often related to the area of solder [51], when there is a pore that reduces the
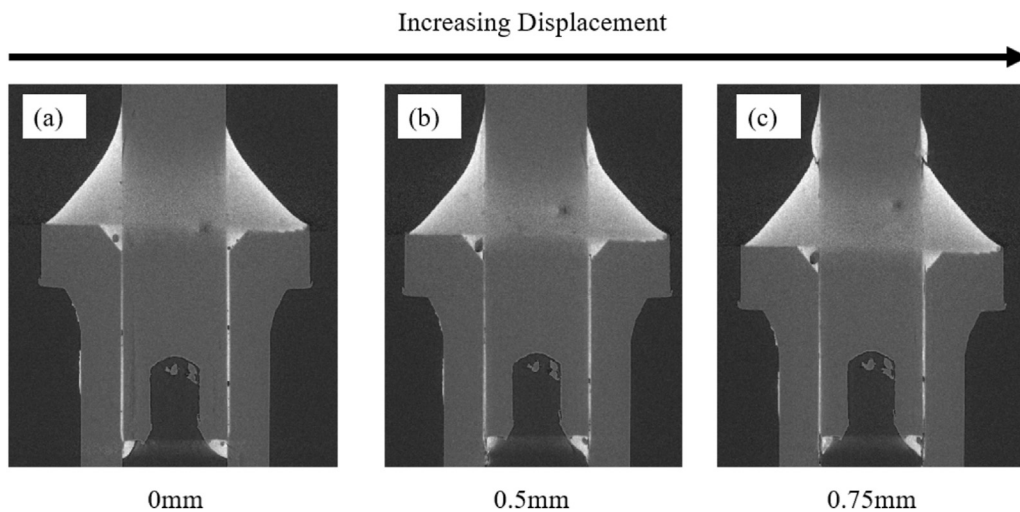

Fig. 11 − SXCT Images of TB2S sample from XZ plane at unloaded state (a), 0.5 mm displacement (b) and 0.75 mm displacement (c).
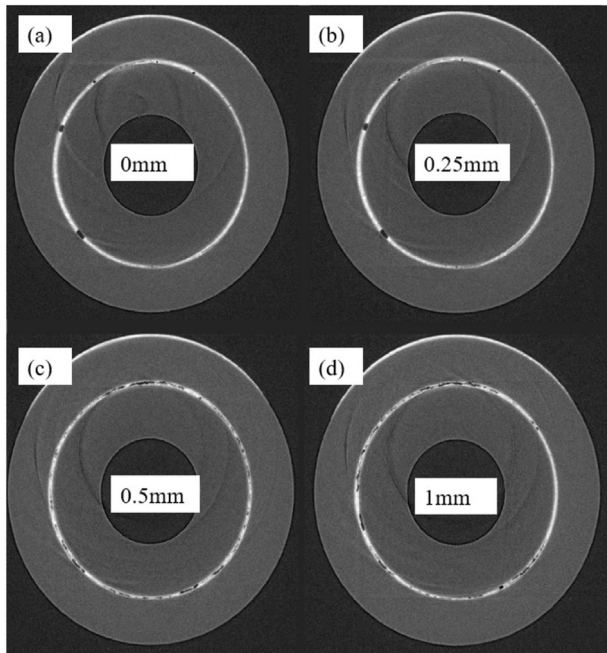
Fig. 12 – SXCT images of TBPS sample from XY Plane, at unloaded state (a), 0.25 mm displacement, (b) 0.5 mm displacement (c) and 1 mm displacement (d).

crack propagation for the TB2S sample was not driven by the porosity levels and the pores did not significantly influence the failure of the solder from cracks travelling between pores.

Analysing the data in a 3D reconstruction, it becomes clearer where the failures occur relative to pores. Fig. 14 shows a 3D comparison of the TBPS solder at 0 mm and 0.5 mm displacements, with a large pore highlighted.

From Fig. 14 it can be seen that the shape of the large pore, circled, does not significantly change between loading. However, the main failure location for the 0.5 mm loaded state occurs at a significant distance away from this large pore. Comparing the failure point with the unloaded image, it appears that the solder was thinner in this region, which may have lead to early failure.

Fig. 15 shows a 3D comparison of the TB2S solder at 0 mm, 0.5 mm and 0.75 mm displacements.

From Fig. 15 it can be seen that several large pores do not change in shape upon loading, and that cracks appear at the base of the solder. Cracks do propagate between some smaller pores, but larger pores, like those highlighted, are unaffected.

3.2. Porosity analysis

The porosity analysis process was carried out at 5 slices along the sample. Fig. 16 shows the percentage porosity levels at each slice for the two samples, and the corresponding number of pores that existed in that slice, for both TBPS and TB2S samples.

As can be seen in Fig. 16, the TB2S sample always has a greater number of pores than the TBPS sample, and an overall much higher percentage porosity. However, there is no clear trend that can be drawn between the number of pores and percentage porosity, indicating that there is a wide range in size of pores.

3.3. SXRD lattice strain interpretation

Following the process of isolating CuNi and solder SXRD peaks described in Section 3.3, horizontal strain maps are presented for both the combined results and the isolated solder peaks for both the TB2S (Figs. 17 and 18 respectively) and TBPS (Figs. 20 and 21 respectively) samples while vertical strain maps are

area of solder it follows that there will be a reduction in strength [26], however this was not observed in this study. In contrast, the reduction in area between pores and centre of the sample appear to have had little effect on crack generation, with cracks originating and propagating along the centre of the solder independently of the presence of pores.

Figs. 12 and 13 show the cross sections in the TBPS sample at the same locations as per the TB2S samples in Figs. 10 and 11. It can be seen that the solder contains significantly fewer pores and that failure occurs at the same displacement level of 0.5 mm. In addition, the cracks propagate in the same location, close to the edge of the inner pipe. This suggests that the
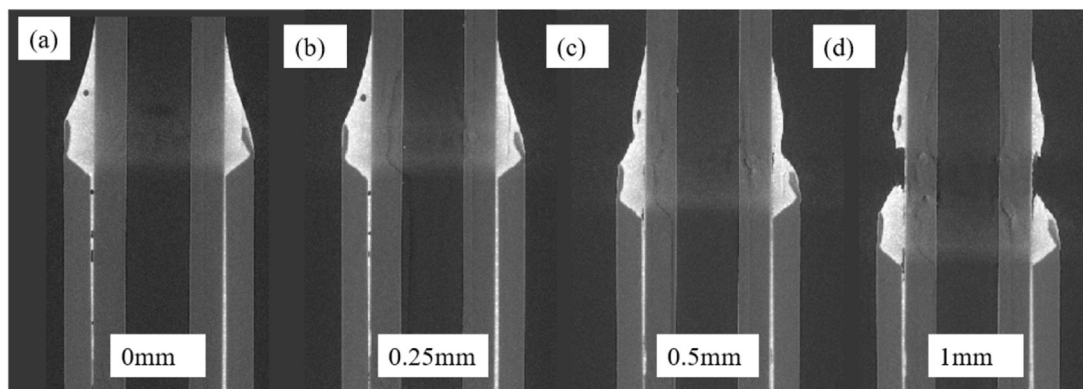

Fig. 13 – SXCT images of TBPS sample from XZ Plane, at unloaded state (a), 0.25 mm displacement, (b) 0.5 mm displacement (c) and 1 mm displacement (d).
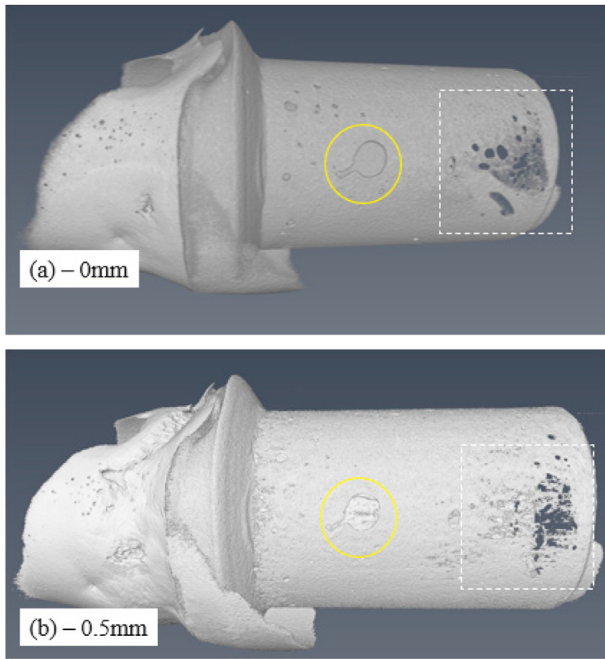
Fig. 14 – 3D reconstruction of TBPS solder showing (a) unloaded state and (b) 0.5 mm displacement.

presented for the combined TB2S sample and TBPS solder (Figs. 19 and 22 respectively).

In both samples, it can be seen that the strains within the solder are higher than the CuNi sleeves (Figs. 17, 19, 20 and 22) in all displacements bar one, the TB2S sample under 0.5 mm loading (Fig. 17). For this sample, the horizontal strains are very high within the CuNi sleeve, before reducing upon further loading. This suggests that horizontally the solder was transferring loads to the grip and had not yet completely failed.

Strains are also present within the solder in an unloaded state (Figs. 17 and 20). This suggests that there are some residual strains present in both samples within the solder from the manufacturing process. To better visualise the locations of residual stresses within the solder, strain maps for both sample types are overlaid onto SXCT images, Fig. 23.

From Fig. 23 it can be seen that the unloaded TB2S sample has strains of up to 0.15%, but negative strains of up to 0.3%. However, the unloaded TBPS sample also has positive strains of up to 0.15% but slightly lower negative strains of 0.2%. Both samples have areas of high strain located within the soldered areas, with variations in positive and negative strains across the solder. These are likely to be residual stresses that exist from the soldering process. Residual stresses are unavoidable in fusion welded components [52] due to the application of external heat to melt the solder. Upon cooling from the liquid state the metal contracts and creates residual stresses which can then expand into the substrate either side as a Heat Affected Zone (HAZ) [53].

Upon loading, the two samples have very different evolutions of strains within the solder. The TBPS sample has very similar strain profiles in both the horizontal and vertical, with distinct areas of high negative and positive strain present across all displacements (Figs. 20 and 22). For the TB2S sample, the horizontal strains are much higher across the sample with particularly high stains seen in the CuNi grip upon loading. For the vertical strains, the locations of high strain are solely located within the solder, with high negative strains seen at the largest displacement. This negative strain of 0.7% is more than double the negative strains seen in the TBPS sample, which only reach a maximum of 0.3%.

The differences in magnitude of strain seen in the TB2S sample compared to the TBPS sample suggests that voiding does cause differences in strains induced upon loading. The differences in strain maps between the vertical and horizontal strain components for the TB2S sample also suggests that voids also influence how stresses are transferred upon loading.

4. Discussion and outlook

While porosity is inevitable for soldered joints, standards that exist for standard sized welds (>0.5 mm) indicate that there is a level of 'acceptable' porosity based on percentage, size and number of pores. This study has found that these do not
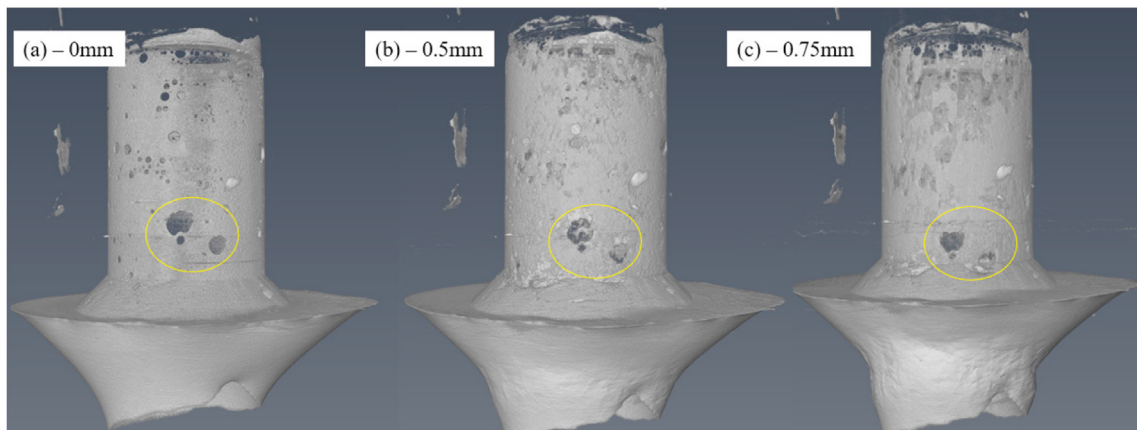

Fig. 15 – TB2S solder at (a) 0 mm, (b) 0.5 mm and (c) 0.75 mm displacements with selected pores highlighted.
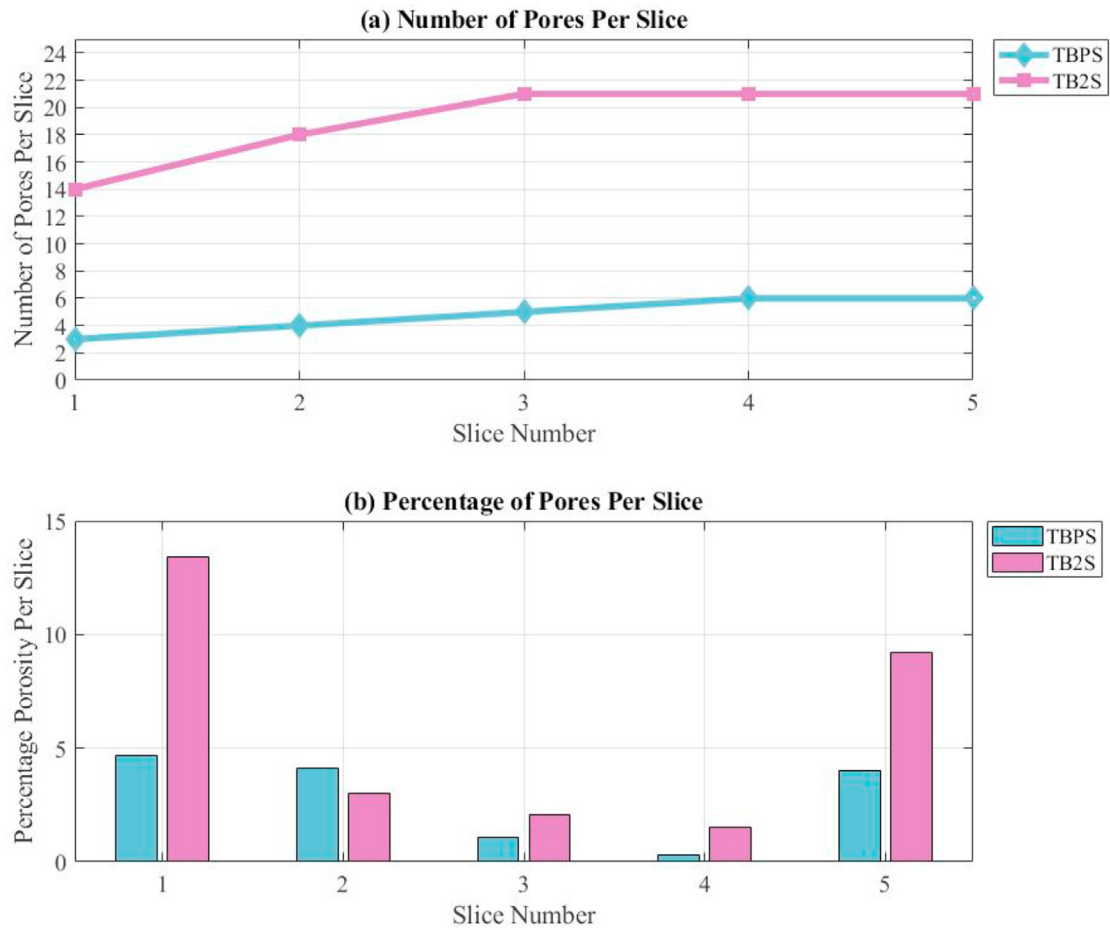
Fig. 16 − Graphs of number of pores per slice (a) and percentage of pores per slice (b) for both TBPS and TB2S samples.
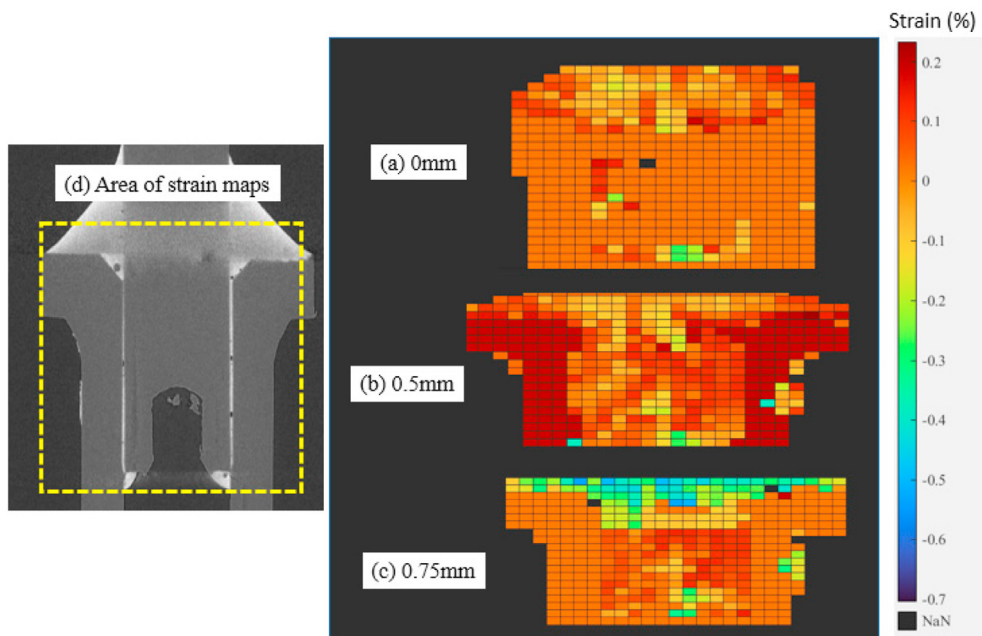

Fig. 17 − Horizontal strain maps for CuNi and solder peaks for TB2S sample at 0 mm displacement (a) 0.5 mm displacement (b) and 0.75 mm displacement (c) with the area of strain maps highlighted on sample geometry (d).

Fig. 18 — Horizontal strain maps for isolated solder peaks for TB2S sample at 0 mm displacement (a) 0.5 mm displacement (b) and 0.75 mm displacement (c) with the area of strain maps highlighted on sample geometry (d).

directly relate to welds for thin-walled pipes (<0.5 mm) as samples with consistently higher percentage, size and number of pores do not fail prematurely to those with less porosity.

In this study, it can be seen that there is a significant difference in strains within the thin solder upon loading, both in terms of magnitude and direction when comparing a sample with significant voids to one with fewer. Within literature, it has been suggested that voids within a solder cause local stress concentrations [54,55] and large pores create local stresses/strains that evolve progressively with deformation [56]. However, other studies have shown that both the shape

Fig. 19 — Vertical strain maps for CuNi and solder peaks for TB2S sample at 0 mm displacement (a) 0.5 mm displacement (b) and 0.75 mm displacement (c) with the area of strain maps highlighted on sample geometry (d).
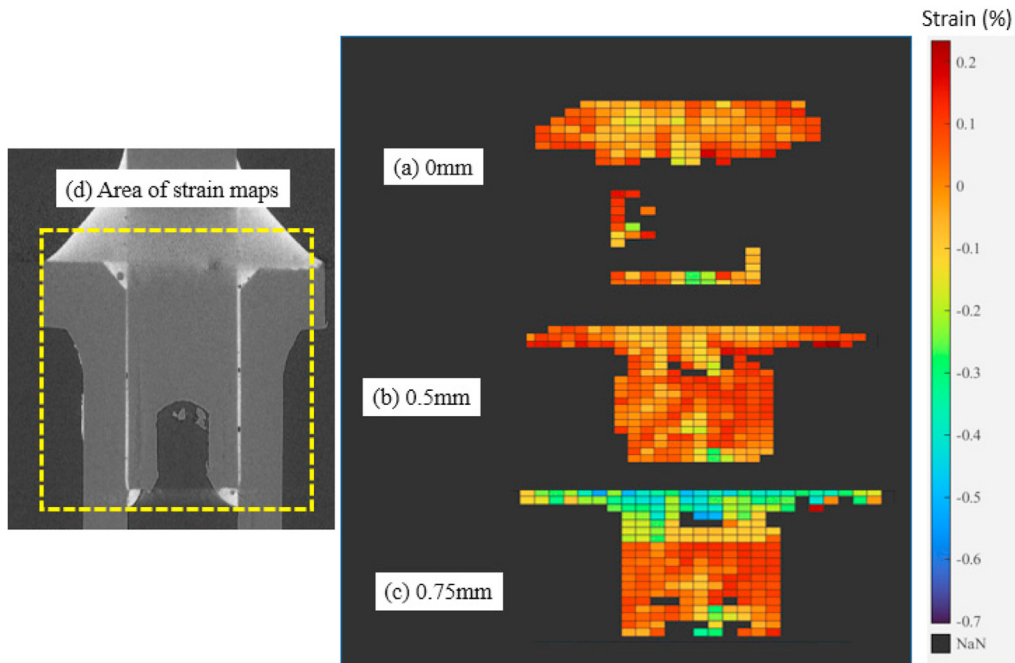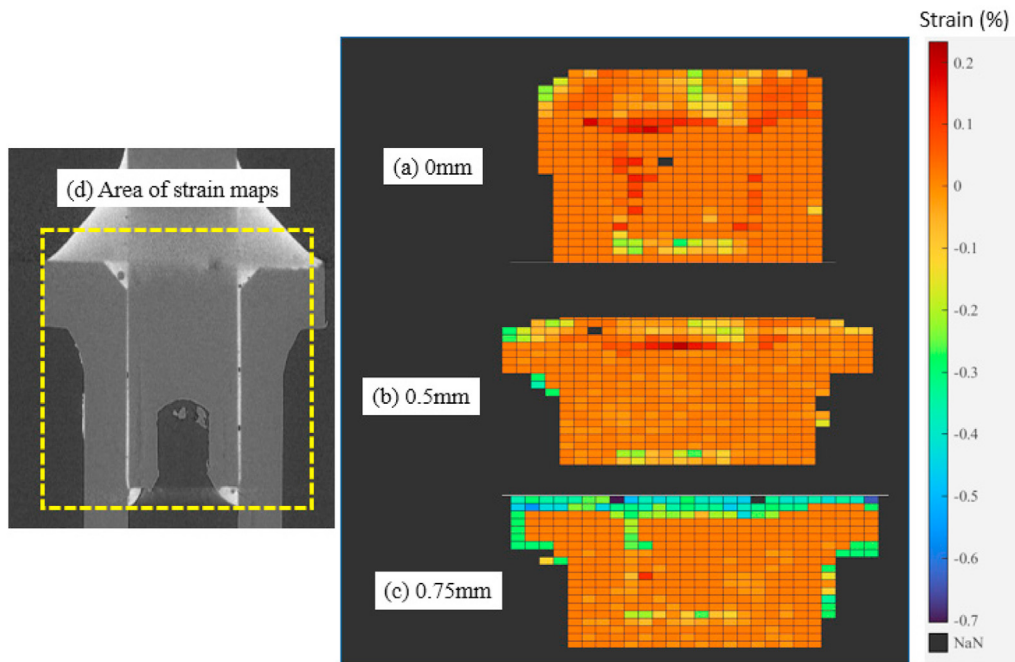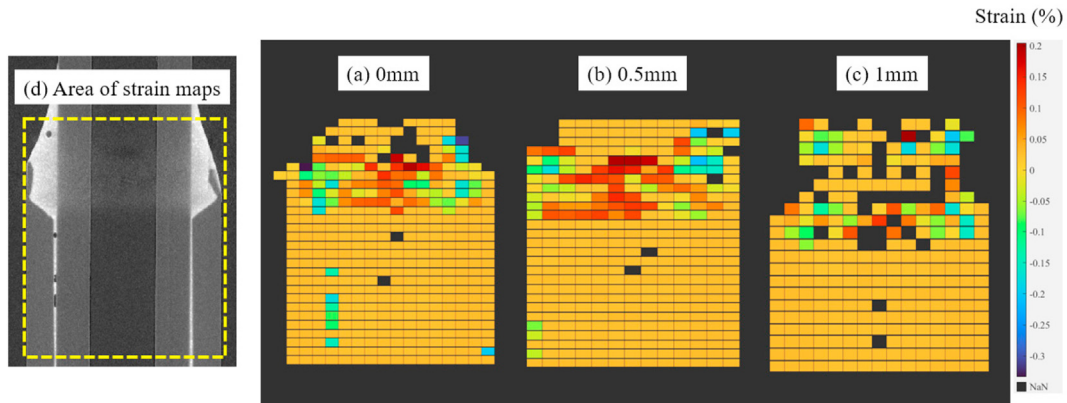
Fig. 20 — Horizontal strain maps for CuNi and solder peaks for TB2S sample at 0 mm displacement (a), 0.5 mm displacement (b) and 1 mm displacement (c) with the area of strain maps highlighted on sample geometry (d).

of a void and the crystallographic orientation of the surrounding material have a strong impact on performance and crack initiation and propagation [57] and as such the size and volume of pores alone may not be an accurate indication of likely performance.

This study has suggested that while voids or porosity do have an effect on the strain induced upon loading, there is not the level of high strain concentrations seen around pores when the solder levels are thicker.

The differences in strain evolution between porous and non-porous samples does not directly relate to early failure, with SXCT images indicating that crack initiation and propagation occurs at the same displacement in both samples. This suggests that the reduction in solder material due to large pores does not affect the overall loading performance for thin soldered joints, and that overall performance is driven by other factors. SXCT images also show that the shape of large

pores is largely unaffected by loading, even when significant failures have occurred in the solder.

Comparing the SXCT images to the SXRD strain maps, it can be seen that areas of higher strain within the porous sample (TB2S) do not directly correlate with crack initiation or failure points. In contrast, strain maps of a soldered sample with lower porosity (TBPS) show localised residual strains at areas of heat application during the soldering process, Figs. 20 and 22. These residual strains correlated directly to the areas of failure in the SXCT data suggesting that residual strains have a direct impact on failure locations for these samples.

Residual stresses are a largely unavoidable phenomenon when fusion welding components, due to the cooling of the liquid solder after joining which has been shown to lead to complicated, inhomogeneous plastic deformations within the solder [58]. The differences in residual stresses between the
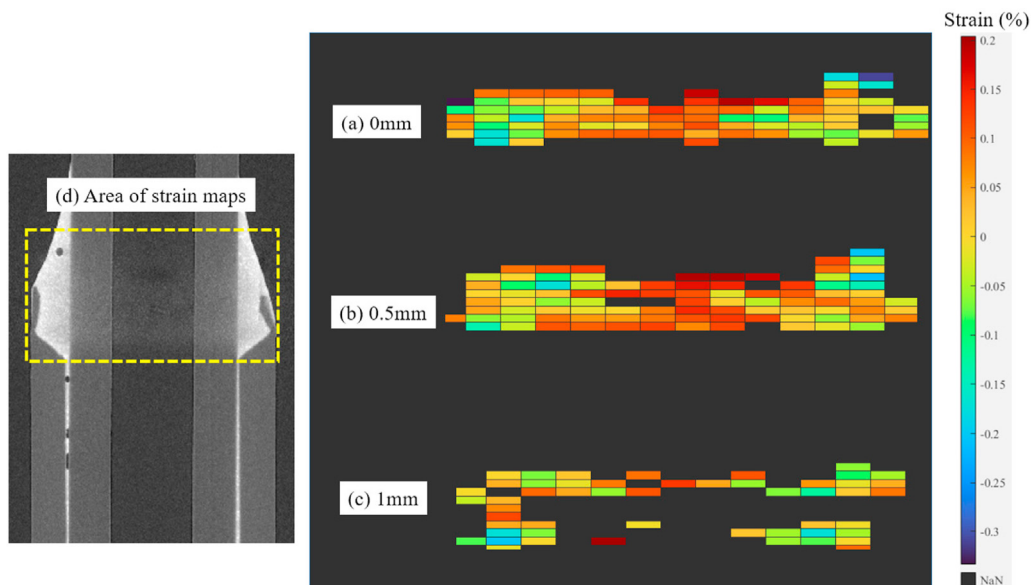

Fig. 21 — Horizontal strain maps for isolated solder peaks for TB2S sample at 0 mm displacement (a), 0.5 mm displacement (b) and 1 mm displacement (c) with the area of strain maps highlighted on sample geometry (d).
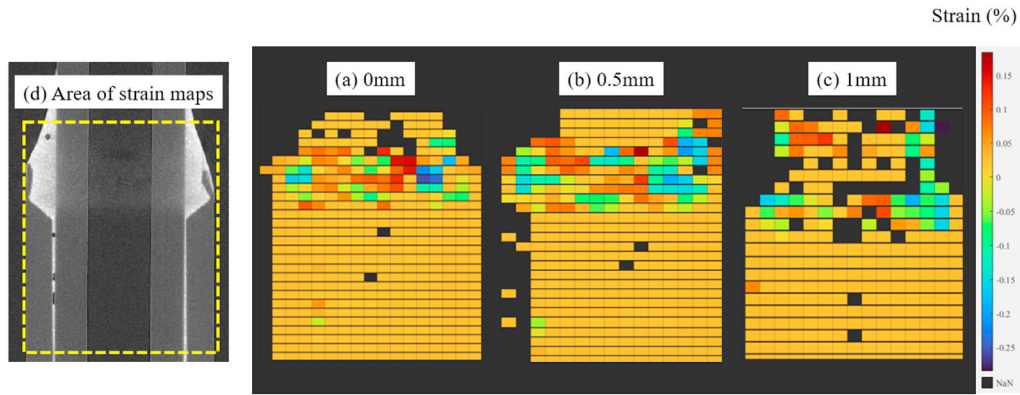
Fig. 22 – Vertical strain maps for CuNi and solder peaks for TB2S sample at 0 mm displacement (a), 0.5 mm displacement (b) and 1 mm displacement (c) with the area of strain maps highlighted on sample geometry (d).
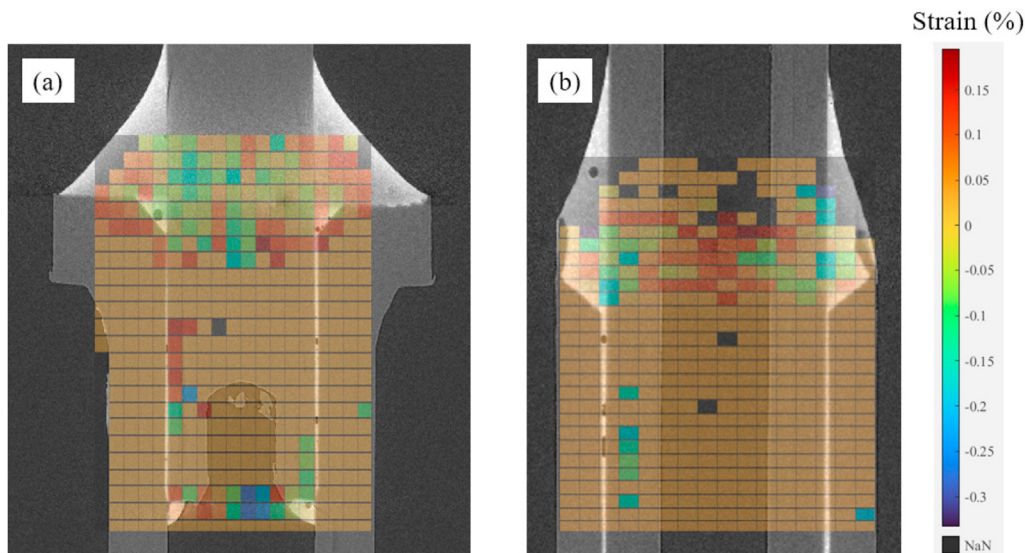

Fig. 23 – Strain Maps for Unloaded (0 mm Displacement) overlaid onto XCT images for (a) TB2S Sample and (b) TBPS Sample.

two samples studied are likely to be caused by the significant changes in geometry for both the solder and supporting material. The TBPS sample likely retained more residual stresses after soldering as the solder was contained within the sleeve and unable to contract after cooling (Fig. 13) whereas the TB2S solder was less contained by the geometry (Fig. 11).

The results of this study serve as an important reference point for a number of ongoing studies. In particular a range of micromechanical test methods are being used to further probe the magnitude and microscale spatial distribution of localised residual stresses at regions of interest. This includes the use of the ring-core focused ion beam and digital image correlation technique [59–61] and nanoindentation/micro-pillar compression across cross-sections of the sample [62]. Further, finite element simulations of the soldering geometry are also being prepared in order to artificially simulate the presence of a range of void distributions, in order to predict the impact of various defect types on the failure load and fatigue properties of the joints [63]. The insights gained from

these further tests and simulations can then be used to alter sample geometry and/or weld parameters to minimise residual stress and maximise joint performance.

5. Conclusions

This work has demonstrated through SXCT imaging and SXRD strain mapping that evolution of strains and failure modes of small-diameter, thin-walled pipe connections are complex, and traditional standards for the characterisation of acceptable porosity levels do not sufficiently determine whether of not a joint will fail prematurely. The main conclusions that can be drawn are as follows:

1. High levels of porosity, up to 10.5% of the total solder area, do not negatively determine the performance when subjected to a progressive tensile displacement, with crack initiation and propagation occurring at the same

displacement as samples with much lower porosity, at a maximum of 4.65% of solder area.

2. Crack initiation and propagation is not driven by porosity and is seen at the same location and loading irrespective of porosity, suggesting that geometry of design is a more important indicator of failure location.

3. Residual stresses are seen within both samples, however the largest residual stress is in tension for the porous sample (maximum strain of 0.15%) and in compression for the less porous sample (maximum strain of 0.3%). From the change in geometry between the two samples, it can be assumed that high compressive strains are a result of less freedom of movement during the cooling process.

4. Stress evolution within the less porous sample was very similar in both horizontal and vertical directions, whereas the more porous sample had very different strain evolutions, with horizontal strains appearing to propagate more evenly through the sample, while vertical strains were isolated on the failure points.

Overall, the above conclusions all indicate that the strain evolution within thin-solder joints are very complex, and while porosity does have an effect on the stresses within the solder, the presence of pores alone cannot predict early failure. To understand the mechanisms which cause early failure of such joints, and in turn create standards to determine an acceptable or unacceptable joint, more work needs to undertaken to characterise the effects of joint geometry and joining parameters on residual stress evolution as this work indicates that crack initiation is driven by residual stresses and not porosity alone.

Funding

Declaration of competing interest

The authors declare that they have no known competing financial interests or personal relationships that could have appeared to influence the work reported in this paper.

REFERENCES

[1] Hartl C. Review on advances in metal micro-tube forming. Metals 2019;9(5). https://doi.org/10.3390/met9050542.

[2] Yi Y, Komine H, Furushima T. Effect of forming conditions on microstructure and room-temperature mechanical characterization of Zn−22Al superplastic microtubes fabricated by direct extrusion. Mater Sci Eng, A 2022;844:143160. https://doi.org/10.1016/j.msea.2022.143160. 2022/06/02/.

[3] Ahamed MS, Saito Y, Mashiko K, Mochizuki M. Characterization of a high performance ultra-thin heat pipe cooling module for mobile hand held electronic devices. Heat Mass Tran 2017;53(11):3241−7. https://doi.org/10.1007/s00231-017-2022-7. 2017/11/01.

[4] Chen X, Ye H, Fan X, Ren T, Zhang G. A review of small heat pipes for electronics. Appl Therm Eng 2016/03/05/ 2016;96:1−17. https://doi.org/10.1016/j.applthermaleng.2015.11.048.

[5] Jin Z, Degang L, Nanan L, Changsheng H. Fatigue analysis of aircraft fuel thin-wall welded tube based on DFR method. Proc SPIE 2022;12244. https://doi.org/10.1117/12.2634874 [Online]. Available:.

[6] Yu H, Li J, He Z. Formability assessment of plastic joining by compression instability for thin-walled tubes. Int J Adv Manuf Technol 2018;97(9):3423−30. https://doi.org/10.1007/s00170-018-2128-1. 2018/08/01.

[7] McNair SAM, et al. Manufacturing technologies and joining methods of metallic thin-walled pipes for use in high pressure cooling systems. Int J Adv Manuf Technol 2022;118(3):667−81. https://doi.org/10.1007/s00170-021-07982-8. 2022/01/01.

[8] Morrison GB, Cassidy D, Johnson J, Sipics M, Wang H, Wolf R. Bonding-induced strain effects in InP DFB components soldered p-side-up on AlN substrates. IEEE JQE 2009;45:937−44. https://doi.org/10.1109/JQE.2009.2016763. 09/01.

[9] Anosov VS, Gomzikov DV, Ichetovkin MI, Seidman LA, Tychkin RI. Study of silicon chip soldering in high-power transistor housing. Mod Electron Mater 2017;3(3):117−21. https://doi.org/10.1016/j.moem.2017.10.004. 2017/09/01/.

[10] Jiang L, Zhang G, Zhou J. Size effects of lead-free solder joint thickness under shear creep based on micro-electrical-resistance strain. J Phys D Appl Phys 2008;41(16):165412. https://doi.org/10.1088/0022-3727/41/16/165412.

[11] Fu H, et al. Ultrasonic-assisted soldering for graphite films as heat sinks with durably superior heat dissipating efficiency. Adv Compos Hybrid Mater 2021. https://doi.org/10.1007/s42114-021-00255-8. 2021/04/22.

[12] Qu W, Zhou S, Zhuang H. Effect of Ti content and Y additions on oxidation behavior of SnAgTi solder and its application on dissimilar metals soldering. Mater Des 2015;88:737−42. https://doi.org/10.1016/j.matdes.2015.09.097. 2015/12/25/.

[13] Gorynin IV, Farmakovsky BV, Vasiliev AF, Vinogradova TS, Samodelkin EA. Activated soldering of dissimilar materials with amorphous solders. Inorg Mater Applied Research 2017;8(6):892−8. https://doi.org/10.1134/S2075113317060053. 2017/11/01.

[14] Wang MS, Wang JY, Chen Q, Peng LM. Fabrication and electrical and mechanical properties of carbon nanotube interconnections. Adv Funct Mater 2005;15(11):1825−31. https://doi.org/10.1002/adfm.200500215. 2005/11/01.

[15] Karamış MB, Taşdemirci A, Nair F. Microstructural analysis and discontinuities in the brazed zone of copper tubes. J Mater Process Technol 2003;141(3):302−12. https://doi.org/10.1016/S0924-0136(03)00281-4. 2003/11/01/.

[16] Siqueira LO, da Silva ACS, Marques IJ, Gonzalez CH, de Abreu Santos TF. Microstructural evaluation of copper brazed joints using silver-based filler metal. Metallogr Microstruct Anal 2021;10(2):174−83. https://doi.org/10.1007/s13632-021-00722-0. 2021/04/01.

[17] Hebda M, Kaczor P, Miernik K. Vacuum brazing of stainless steel depending on the surface preparation method and temperature of the process. Arch Metall Mater 2019;64:5−11. https://doi.org/10.24425/amm.2019.126210. 01/01.

[18] Hou H, Lu D, Zhang S, Zhang Y, Cheng C. Research on on-line ultrasonic testing of small diameter thin wall stainless steel

straight welded pipe. J Phys Conf 2021;1820(1):012086. https://doi.org/10.1088/1742-6596/1820/1/012086. 2021/03/01.

[19] BS En Iso. Welding. Fusion-welded joints in steel, nickel, titanium and their alloys (beam welding excluded). Quality levels for imperfections. British Standards Institute; 2014.

[20] BS En Iso. Electron and laser-beam welded joints. Requirements and recommendations on quality levels for imperfections. Steel nickel titanium and their alloys 2019.

[21] BS EN ISO. Electron and laser-beam welded joints. Requirements and recommendations on quality levels for imperfections. Aluminium magnesium and their alloys and pure copper 2021.

[22] Hu Y, et al. Inhibiting weld cracking in high-strength aluminium alloys. Nat Commun 2022;13(1):5816. https://doi.org/10.1038/s41467-022-33188-x. 2022/10/03.

[23] Pantazică M, Svasta P, Wohlrabe H, Wolter KJ. Factors influencing the formation of voids in chip component solder joints. In: 2013 IEEE 19th International Symposium for Design and Technology in Electronic Packaging (SIITME), 24–27 Oct. 2013; 2013. p. 277–82. https://doi.org/10.1109/SIITME.2013.6743690.

[24] Cheng S, Huang C-M, Pecht M. A review of lead-free solders for electronics applications. Microelectron Reliab 2017/08/01/2017;75:77–95. https://doi.org/10.1016/j.microrel.2017.06.016.

[25] Otiaba KC, Okereke MI, Bhatti RS. Numerical assessment of the effect of void morphology on thermo-mechanical performance of solder thermal interface material. Appl Therm Eng 2014;64(1):51–63. https://doi.org/10.1016/j.applthermaleng.2013.12.006. 2014/03/01/.

[26] Xinmeng Z, et al. Effect of soldering temperature on the reliability of Sn-Ag-Cu lead-free solder joints. J Electron Mater 2021;50(3):869–80. https://doi.org/10.1007/s11664-020-08715-5. 2021/03/01.

[27] Yunus M, Primavera A, Srihari K, Pitarresi JM. Effect of voids on the reliability of BGA/CSP solder joints. In: Twenty Sixth IEEE/CPMT International Electronics Manufacturing Technology Symposium (Cat. No.00CH37146), 3–3 Oct. 2000; 2000. p. 207–13. https://doi.org/10.1109/IEMT.2000.910730.

[28] Ali A, Chiang YW, Santos RM. X-Ray diffraction techniques for mineral characterization: a review for engineers of the fundamentals, applications, and Research directions. Minerals 2022;12(2). https://doi.org/10.3390/min12020205.

[29] Brokmeier H-G. Hard X-rays for in situ strain and texture measurements. Part Part Syst Char 2009;26(3):117–24. https://doi.org/10.1002/ppsc.200800050.

[30] Serrano-Munoz I, Roveda I, Kupsch A, Müller BR, Bruno G. Synchrotron X-ray refraction detects microstructure and porosity evolution during in-situ heat treatments. Mater Sci Eng, A 2022;838:142732. https://doi.org/10.1016/j.msea.2022.142732. 2022/03/24/.

[31] Sun W, et al. Review of high energy x-ray computed tomography for non-destructive dimensional metrology of large metallic advanced manufactured components. Rep Prog Phys 2022;85(1):016102. https://doi.org/10.1088/1361-6633/ac43f6. 2022/01/01.

[32] Turpin L, Roux S, Caty O, King A, Denneulin S, Martin É. In situ tomographic study of a 3D-woven SiC/SiC composite part subjected to severe thermo-mechanical loads. J Synchrotron Radiat 2022;29(Pt 2):522–31. https://doi.org/10.1107/s1600577522000406.

[33] Wu SC, Xiao TQ, Withers PJ. The imaging of failure in structural materials by synchrotron radiation X-ray microtomography. Eng Fract Mech 2017;182:127–56. https://doi.org/10.1016/j.engfracmech.2017.07.027. 2017/09/01/.

[34] Daguin J, Noite J, Petagna P, Postema H, Tropea P, Verlaat B. Evaporative CO2 cooling system for the upgrade of the CMS Pixel detector at CERN. 2012.

[35] Delcourt M. The CMS tracker upgrade for the high luminosity LHC. Nucl Instrum Methods Phys Res Sect A Accel Spectrom Detect Assoc Equip 2019;936:621–4. https://doi.org/10.1016/j.nima.2018.11.023. 2019/08/21/.

[36] Benhadid-Dib S, Benzaoui A. Refrigerants and their environmental impact Substitution of hydro chlorofluorocarbon HCFC and HFC hydro fluorocarbon. Search for an adequate refrigerant. Energy Proc 2012;18:807–16.

[37] A. L. Rosa, "The CMS outer tracker for the high luminosity LHC upgrade," J Instrum, vol. 15, no. 02, pp. C02029, 2020/02/19 2020, doi: 10.1088/1748-0221/15/02/c02029.

[38] Filik J, et al. Processing two-dimensional X-ray diffraction and small-angle scattering data in DAWN 2. J Appl Crystallogr 2017;50(3):959–66. https://doi.org/10.1107/S1600576717004708.

[39] Basham M, et al. Data analysis WorkbeNch (DAWN). J Synchrotron Radiat 2015;22(3):853–8. https://doi.org/10.1107/S1600577515002283.

[40] Pednekar PP, Godiyal SC, Jadhav KR, Kadam VJ. Chapter 23 - mesoporous silica nanoparticles: a promising multifunctional drug delivery system. In: Ficai A, Grumezescu AM, editors. Nanostructures for cancer therapy. Elsevier; 2017. p. 593–621.

[41] Selva TMG, Selva JSG, Prata RB. Sensing materials: diamond-based materials. In: Reference module in biomedical sciences. Elsevier; 2021.

[42] Raval N, Maheshwari R, Kalyane D, Youngren-Ortiz SR, Chougule MB, Tekade RK. Chapter 10 - importance of physicochemical characterization of nanoparticles in pharmaceutical product development. In: Tekade RK, editor. Basic fundamentals of drug delivery. Academic Press; 2019. p. 369–400.

[43] Ida T, Ando M, Toraya H. Extended pseudo-voigt function for approximating the voigt profile. J. Appl. Cryst 2000;33. https://doi.org/10.1107/S0021889800010219. 12/01.

[44] Bhat R, Bekal S, Hegde A. Fabrication of Zn-Ni alloy coatings from acid chloride bath and its corrosion performance. Anal Bioanal Electrochem 2018;10:1562–73. 12/31.

[45] Marenych O, Kostryzhev A. Strengthening mechanisms in nickel-copper alloys: a review. Metals 2020;10(10). https://doi.org/10.3390/met10101358.

[46] Alaf M, Gultekin D, Akbulut H. Tin/tinoxide (Sn/SnO 2) nanocomposites thin films as negative-electrode materials for Li-ion batteries. Acta Phys Pol, A 2013;123:323–5. https://doi.org/10.12693/APhysPolA.123.323. 02/01.

[47] Atwood RC, Bodey AJ, Price SWT, Basham M, Drakopoulos M. A high-throughput system for high-quality tomographic reconstruction of large datasets at diamond light source. Phil Trans Math Phys Eng Sci 2015;373(2043). https://doi.org/10.1098/rsta.2014.0398. Art no. 20140398.

[48] McLoughlin S, Mays C. Synchrotron X-ray imaging reveals the three-dimensional architecture of beetle borings (Dekosichnus meniscatus) in Middle–Late Jurassic araucarian conifer wood from Argentina. Rev Palaeobot Palynol 2022;297:104568. https://doi.org/10.1016/j.revpalbo.2021.104568. 2022/02/01/.

[49] Gjesteby L, et al. Metal artifact reduction in CT: where are we after four decades? IEEE Access 2016;4:5826–49. https://doi.org/10.1109/access.2016.2608621.

[50] Glinz J, Zabler S, Kastner J, Senck S. Metal artifacts in attenuation and phase contrast X-ray microcomputed tomography: a comparative study. Exp Mech 2022. https://doi.org/10.1007/s11340-022-00835-9.

[51] Jiang C, et al. Effects of voids on mechanical and thermal properties of the die attach solder layer used in high-power LED chip-scale packages. IEEE Trans Compon Packag Manuf

Technol 2018;8(7):1254–62. https://doi.org/10.1109/TCPMT.2018.2789345.

[52] Tornqvist R, Wang J, Tronskar J, Sisan A. Welding residual stress and pipeline integrity. 2014.

[53] R. W. Revie, "7. Residual stress in pipelines," in Oil and gas pipelines - integrity and safety handbook: John Wiley & Sons..

[54] Vanderesse N, Maire É, Chabod A, Buffière JY. Microtomographic study and finite element analysis of the porosity harmfulness in a cast aluminium alloy. Int J Fatig 2011;33(12):1514–25. https://doi.org/10.1016/j.ijfatigue.2011.06.010. 2011/12/01/.

[55] Nicoletto G, Konečná R, Fintova S. Characterization of microshrinkage casting defects of Al–Si alloys by X-ray computed tomography and metallography. Int J Fatig 2012;41:39–46. https://doi.org/10.1016/j.ijfatigue.2012.01.006. 2012/08/01/.

[56] Zhang Y, et al. Analysis of local stress/strain fields in an HPDC AM60 plate containing pores with various characteristics. Eng Fail Anal 2021;127:105503. https://doi.org/10.1016/j.engfailanal.2021.105503. 2021/09/01/.

[57] Diehl M, Wicke M, Shanthraj P, Roters F, Brueckner-Foit A, Raabe D. Coupled crystal plasticity–phase field fracture simulation study on damage evolution around a void: pore shape versus crystallographic orientation. JOM (J Occup Med) 2017;69(5):872–8. https://doi.org/10.1007/s11837-017-2308-8. 2017/05/01.

[58] Bing K, Eigenmann B, Scholtes B, Macherauch E. Brazing residual stresses in components of different metallic materials. Mater Sci Eng, A 1994;174(1):95–101. https://doi.org/10.1016/0921-5093(94)91116-9. 1994/01/01/.

[59] Lunt AJG, et al. A state-of-the-art review of micron-scale spatially resolved residual stress analysis by FIB-DIC ring-core milling and other techniques. J Strain Anal Eng Des 2015;50(7):426–44. https://doi.org/10.1177/0309324715596700. 2015/10/01.

[60] Lunt AJG, Salvati E, Ma L, Dolbnya IP, Neo TK, Korsunsky AM. Full in-plane strain tensor analysis using the microscale ring-core FIB milling and DIC approach. J Mech Phys Solid 2016;94:47–67. https://doi.org/10.1016/j.jmps.2016.03.013. 2016/09/01/.

[61] Lunt AJG, Korsunsky AM. A review of micro-scale focused ion beam milling and digital image correlation analysis for residual stress evaluation and error estimation. Surf Coating Technol 2015;283:373–88. https://doi.org/10.1016/j.surfcoat.2015.10.049. 2015/12/15/.

[62] Lunt AJG, et al. A comparative transmission electron microscopy, energy dispersive x-ray spectroscopy and spatially resolved micropillar compression study of the yttria partially stabilised zirconia - porcelain interface in dental prosthesis. Thin Solid Films 2015;596:222–32. https://doi.org/10.1016/j.tsf.2015.07.070. 2015/12/01/.

[63] Xu ZW, Wu SC, Wang XS. Fatigue evaluation for high-speed railway axles with surface scratch. Int J Fatig 2019;123:79–86. https://doi.org/10.1016/j.ijfatigue.2019.02.016. 2019/06/01/.